

# The particle content of low-power radio galaxies in groups and clusters

J. H. Croston<sup>1\*</sup> and M.J. Hardcastle<sup>2</sup>

<sup>1</sup> School of Physics and Astronomy, University of Southampton, Highfield, Southampton SO17 1BJ, UK

<sup>2</sup> School of Physics, Astronomy and Mathematics, University of Hertfordshire, College Lane, Hatfield, Hertfordshire AL10 9AB, UK

27 September 2018

## ABSTRACT

The synchrotron-radiating particles and magnetic fields in low-power radio galaxies (including most nearby cluster-centre sources), if at equipartition, can provide only a small fraction of the total internal energy density of the radio lobes or plumes, which is now well constrained via X-ray observations of their external environments. We consider the constraints on models for the dominant energy contribution in low-power radio-galaxy lobes obtained from a detailed comparison of how the internal equipartition pressure and external pressure measured from X-ray observations evolve with distance for two radio galaxies, 3C 31 and Hydra A. We rule out relativistic-lepton dominance of the radio lobes, and conclude that models in which magnetic field or relativistic protons/ions carried up the jet dominate lobe energetics are unlikely. Finally, we argue that entrainment of material from the jet surroundings can provide the necessary pressure, and construct a simple self-consistent model of the evolution of the entrainment rate required for pressure balance along the 100-kpc scale plumes of 3C 31. Such a model requires that the entrained material is heated to temperatures substantially above that of the surrounding intra-group medium, and that the temperature of the thermal component of the jet increases with distance, though remaining sub-relativistic.

**Key words:** galaxies: active – X-rays: galaxies: clusters

## 1 INTRODUCTION

Low-power (FRI: Fanaroff & Riley 1974) radio galaxies are commonly found in the centres of rich galaxy groups and clusters, where they are thought to play an important role in regulating the central gas properties and galaxy evolution via a (currently poorly understood) feedback process (e.g. McNamara & Nulsen 2007; Fabian 2012, and references therein). Among the many uncertainties about the way in which this feedback process operates, one long-standing problem is the unknown nature of the dominant particle or field component within the radio lobes, which are important as the lobes are the means of energy transfer to the surrounding gas via their expansion. The radio synchrotron emission from the lobes provides only a combined constraint on electron density and magnetic field strength, and so it has been common to assume equipartition of energy in field and radiating particles (e.g. Burbidge 1956), which corresponds roughly to the minimum total energy the source requires in order to produce the observed radio emission. But while the lobes of powerful FRII radio galaxies appear to be close to equipartition (e.g. Croston et al. 2005; Kataoka & Stawarz 2005), it has been known for some time that the energy content of FRI radio galaxies must be distributed differently to that of FRIIs, as the

radiating particles and magnetic field, if at equipartition, cannot in the vast majority of cases provide sufficient pressure to balance the measured external pressures surrounding FRI lobes (e.g. Morganti et al. 1988; Worrall & Birkinshaw 2000).

The external pressure acting on the jets and lobes can now be constrained tightly on scales of a few to several hundred kpc for many low-power radio galaxies, using X-ray observations of the surrounding group or cluster gas with *Chandra* and *XMM-Newton* (e.g. Hardcastle et al. 2002; Croston et al. 2003, 2008). If it is assumed that the jets and lobes are close to pressure equilibrium with the surrounding medium (likely to be true on kpc – hundred kpc scales for low-power sources), then the external pressure profile must correspond closely to the run of internal pressure along the jet as it evolves into a lobe or plume. The internal pressure cannot be measured directly from the radio observations of the source; however, the internal pressure in some combination of radiating particles (electrons and positrons) and magnetic field can be measured by modelling the radio emission. This type of comparison has now been carried out for many low-power radio galaxies, including large samples of cavity sources in galaxy clusters (including so-called “ghost” cavities in which any radio emission is weak or absent), and, as mentioned above, typically shows that the radiating particles and magnetic field cannot dominate the internal energy of

\* Email: J.Croston@soton.ac.uk

the source *if they are at equipartition* (Croston et al. 2003, 2008; Dunn & Fabian 2004; Dunn et al. 2005, 2006; Bîrzan et al. 2008).

Given that the lobes of low-power radio galaxies cannot be dominated by an equipartition electron-positron plasma, other models for the energetically dominant component of the radio lobe contents must be considered. The two most obvious explanations are that the dominant internal pressure is provided by a departure from equipartition or by a significant population of non-radiating particles. There is evidence from X-ray inverse Compton observations that powerful FR II radio galaxies may deviate from equipartition by a small amount in the direction of electron dominance (e.g. Isobe et al. 2002; Croston et al. 2005); however, electron dominance by large factors would be expected to produce detectable levels of X-ray inverse-Compton emission in at least some FRI radio galaxies, which are inconsistent with observations (Hardcastle et al. 1998; Croston et al. 2003). Recently, detailed models of magnetically dominated jets and lobes have been developed (e.g. Li et al. 2006; Nakamura et al. 2006); however, they are difficult to reconcile with observations, e.g. of radio jet polarization properties and geometry (see later discussion). Proton-dominated models have been discussed by a number of authors (e.g. De Young 2006; Bîrzan et al. 2008; McNamara & Nulsen 2007), but it is energetically difficult to supply the proton population required by transport from the inner jet (e.g. De Young 2006).

There are several reasons to favour instead a model in which entrainment of material as the jet expands leads to an energetically dominant proton population on scales of tens to hundreds of kpc. Entrainment of the ISM and ICM is thought to be the means by which FRI jets decelerate from relativistic to transonic speeds on kpc scales (e.g. Bicknell 1994). There is growing observational evidence that entrainment is occurring (e.g. Hardcastle et al. 2003, 2007), as well as strong support for its importance from detailed kinematic modelling of FRI jets (e.g. Laing & Bridle 2002; Laing et al. 2006). A model in which entrainment accounts for the apparent “missing” pressure in FRI radio galaxies also has the advantage of explaining the observed difference in the energetics of the FRI and FR II populations (the former being massively underpressured if at equipartition, while the latter appear close to equipartition both from IC observations and pressure comparisons) without the need to invoke differences in the intrinsic particle content of the inner jets, which might require different jet production mechanisms: since FR II jets do not decelerate or interact with their environments significantly, they would not in general be expected to entrain significant amounts of material. Finally, we have previously found a relationship between FRI source structure and particle/energy content, suggesting that sources likely to be undergoing strong entrainment have a larger contribution from non-radiating material than those likely to be weakly entraining (Croston et al. 2008). This provides further support for an entrainment-dominated model.

In this paper we investigate in detail the observational constraints on models for the particle and energy content of low-power radio galaxies, by considering how the non-radiating and radiating components of the jets in the well-studied radio galaxy 3C 31 must evolve with distance in order to maintain pressure balance and produce the observed radio emission. We use new deep X-ray data and high-resolution radio data to place tight constraints on the external pressure and internal pressure from radiating particles and field within the radio jets and plumes of 3C 31. We consider in detail the constraints this result provides for what particle population or magnetic field structure dominates the source energetics, and also carry out a pressure comparison for the cluster-centre source Hydra A as a preliminary test of the generality of our results.

Throughout the paper we use a cosmology in which  $H_0 = 70 \text{ km s}^{-1} \text{ Mpc}^{-1}$ ,  $\Omega_m = 0.3$  and  $\Omega_\Lambda = 0.7$ . At the redshifts of 3C 31 ( $z = 0.0169$ ) and Hydra A ( $z = 0.0549$ ), this gives luminosity distances of  $D_L = 73.3 \text{ Mpc}$  and  $D_L = 244.9 \text{ Mpc}$ , respectively, and angular scales of  $0.3438 \text{ kpc/arcsec}$  (3C 31) and  $1.067 \text{ kpc/arcsec}$  (Hydra A). Spectral indices  $\alpha$  are defined in the sense  $S_\nu \propto \nu^{-\alpha}$ . Reported errors are  $1\sigma$  for one interesting parameter, except where otherwise noted.

## 2 OBSERVATIONAL CONSTRAINTS

### 2.1 External pressure of the hot-gas environment

#### 2.1.1 3C 31

We used new *XMM-Newton* data to obtain a radial profile of the external pressure surrounding the radio jets and plumes in 3C 31. We observed 3C 31 on 2008 July 1st for  $\sim 50 \text{ ks}$  (ObsID 0551720101). The data were processed in the standard way using *XMM-Newton* SAS version 11.0.0, and the latest calibration files from the *XMM-Newton* website. The pn data were filtered to include only single and double events ( $\text{PATTERN} \leq 4$ ), and  $\text{FLAG} = 0$ , and the MOS data were filtered according to the standard flag and pattern masks ( $\text{PATTERN} \leq 12$  and  $\#\text{XMMEA\_EM}$ , excluding bad columns and rows). Unfortunately the observation was badly affected by background flares, and so after filtering for good time intervals, the remaining clean exposure durations were 24, 29, and 24 ks for the MOS1, MOS2 and pn cameras, respectively.

Surface brightness profiles in the energy range  $0.3 - 5.0 \text{ keV}$  were extracted from the *XMM-Newton* data using the closed-filter double-background method described by Croston et al. (2008). The *Chandra* surface brightness profile of Hardcastle et al. (2002) was also used to help constrain the inner profile shape. The combined *XMM-Newton* (MOS1, MOS2 and pn) profile and *Chandra* profile were jointly fitted with a projected double beta model (Croston et al. 2008), convolved with the appropriate point-spread function (PSF) for each telescope, using the Markov-Chain Monte Carlo (MCMC) method described by Ineson et al. (2013). The resulting model was used to obtain a gas density profile for the environment.

A corresponding temperature profile was obtained by extracting spectra from six annular regions, and using the background fitting method described by Croston et al. (2008), which correctly accounts for both particle and X-ray background, to obtain (projected) temperature measurements. For each region, the spectra from the three *XMM-Newton* cameras were fitted jointly with an *apec* model (using the energy range  $0.3 - 7.0 \text{ keV}$ , but excluding the region between  $1.4 - 1.6 \text{ keV}$ , which is affected by an instrumental line). The normalizations for the three cameras were allowed to vary, but the temperatures were tied together. A free abundance fit led to unphysically large values for the abundance, and so we fixed the abundance to the best-fitting abundance from a global spectral fit ( $Z = 0.3$ ). The results of spectral fitting are given in Table 1. For the inner regions of the group, we used the *Chandra* temperature profile of Hardcastle et al. (2002) in order to obtain more accurate pressure constraints. We used the deprojected temperature values, although the effect of deprojection on the temperature profile is small. In the outer regions of the group the temperature varies only by  $\sim 20$  per cent, so that any uncertainty from not correcting for projection is small, and less than the statistical uncertainty on the outer temperature.

In order to obtain a gas pressure profile with high resolution, we fitted the measured temperature profile with the analytic model

**Table 1.** Results of spectral fitting for the environment of 3C 31. Spectral fits were obtained for annular regions between the radii listed, using an APEC model, were in the energy range 0.3 – 7 keV, assuming  $N_H = 5.4 \times 10^{20} \text{ cm}^{-2}$ . The abundance was fixed to the best-fitting value from a global spectral fit, as free abundance fits led to unphysical values (likely due to the additional free parameters of the background model).

Region	$kT$	$Z$	$\chi^2$ (d.o.f.)
60 – 80 arcsec	$1.58 \pm 0.1$	0.1	64 (65)
80 – 120 arcsec	$1.62^{+0.6}_{-0.7}$	0.3	157 (167)
120 – 200 arcsec	$1.60^{+0.5}_{-0.6}$	0.3	466 (395)
200 – 300 arcsec	$1.54 \pm 0.5$	0.3	722 (608)
300 – 450 arcsec	$1.36^{+0.2}_{-0.1}$	0.3	1046 (835)
450 – 600 arcsec	$1.09^{+0.12}_{-0.01}$	0.3	1191 (974)

of Vikhlinin et al. (2006), and obtained a finely binned look-up table for  $\Lambda(T)$ , the conversion factor between volume emission measure and gas density (obtained from XSPEC). The resulting table was used together with the analytic temperature model to obtain a gas pressure profile, which is shown in Fig 1.

### 2.1.2 Hydra A

Although the majority of this paper focuses on 3C 31, using our new X-ray data, we also carried out a pressure comparison for Hydra A as a preliminary test of whether our findings are likely to apply widely to FRI radio galaxies. For Hydra A, we did not re-analyse the archival *Chandra* and *XMM-Newton* observations, but made use of previously published gas density and temperature profiles. For the gas density profile we used the double beta model of Wise et al. (2007), normalised to the density profile published by David et al. (2001). We interpolated over the (projected) temperature profile of David et al. (2001) to obtain a cluster pressure profile over the radial ranges of interest, which is also shown in Fig. 1.

## 2.2 Internal pressure from radiating particles and magnetic field

The radio emission from the sources does not place a constraint on the total internal pressure of the lobes, as the radiating plasma could be far from equipartition; however, it does place constraints on the internal pressure of the radiating particles and magnetic field. We used high-resolution radio data to obtain profiles of synchrotron emissivity along the jets.

For 3C 31 we used the combined 1.4-GHz map of Laing et al. (2008), which has a resolution of 5 arcsec, and a 330-MHz map made in the standard way from VLA archival data in the B and C configurations (Program AL597), with a resolution of 21.3 arcsec  $\times$  18.2 arcsec, to obtain the most reliable low-frequency measurements for outer regions. These data enable us to measure the source geometry and radio surface brightness accurately in the inner regions, while adequately sampling the source structure out to the hundred kpc scale regions of interest. For Hydra A we used the 330-MHz map of Laing & Bridle (2004) for the outer lobes with a resolution of 15 arcsec, and to image the inner structure with sufficient resolution for our geometric measurements we made a map using A and B configuration archival VLA data at 1.4 GHz (e.g. Taylor et al. 1990) with resolution of 1.4 arcsec. For 3C 31, roughly 20 regions per jet were used to measure the radio flux density and jet geometry. For Hydra A around 20 regions were used

to study the northern jet. In the case of 3C 31, where significant jet bending occurs on the scales of interest, we measured the distances along the projected jet paths as the best way of estimating the distance travelled by material at a particular position along the jet; however, for simplicity we assumed initially the source is in the plane of the sky, and does not change position angle relative to the plane. The external pressure acting at a particular position is therefore assumed to be the pressure at the distance corresponding to the projected radial distance from the AGN nucleus and group centre. The effects of projection and jet bending on our results are discussed in Section 3.4.

To investigate the energetics of the radiating particles and magnetic field, we initially assumed a single electron energy distribution consisting of a power law with spectral index of 0.55, minimum electron energy of  $\gamma = 10$  and maximum energy of  $\gamma = 10^4$ . This correctly describes the radio spectra of the two sources in the inner regions (in the GHz radio regime), but is a somewhat flatter spectral index than is measured in the outer parts of the source. Any systematic effects of spectral steepening at GHz frequencies on our pressure results for the outer parts of the sources will be small, as the total electron energy content is dominated by the low-energy electron population. Allowing the spectral index to vary based on the observed spectral index at GHz frequencies would introduce large systematic uncertainty in the low-energy electron density. We therefore used a single electron distribution for all regions, normalised to the measured radio flux density for that region from the appropriate radio map (in the case of Hydra A flux densities at 5 GHz were used in order to have sufficient spatial resolution out to a distance of 40 kpc, with the 330-MHz map used beyond that distance). In future work we will make use of new low-frequency data from the Low-Frequency Array (LOFAR) to improve our spectral model.

In order to investigate the variations in internal conditions along the source, a power law was fitted to the emissivity distribution so as to provide a smooth model for the variation with distance. Although there is some small systematic deviation of the observed emissivity about the model, the measured profile is never more than  $\sim 40$  percent different from the model (and typically within 10 percent).

Using the smoothed emissivity profiles for 3C 31, we first determined the internal pressure as a function of position along the jet, under the assumptions of equipartition of energy between particles and magnetic field, and no non-radiating particles ( $\kappa = 0$ , where  $\kappa = U_{NR}/U_R$ , i.e. the ratio of energy density in non-radiating particles to that in synchrotron-emitting particles). The internal, equipartition pressure profiles for are shown in Fig. 1, together with the external pressure profiles determined from the X-ray observations. For Hydra A, we simply calculated an internal pressure profile for the existing radio bins, under the same assumptions. This profile is shown in Fig. 1, illustrating a strong qualitative similarity to the behaviour of the 3C 31 jets.

## 3 IMPLICATIONS FOR LOBE CONTENTS

Fig. 2 shows the ratio of external pressure to internal, equipartition pressure (with no protons) for 3C 31, determined from the external and internal pressure profiles described in the previous section. As seen in previous work (e.g. Worrall & Birkinshaw 2000), the internal equipartition pressure is significantly below the external pressure at all radii. It also is readily apparent that the apparent pressure “deficit” increases with distance, apart from in the inner

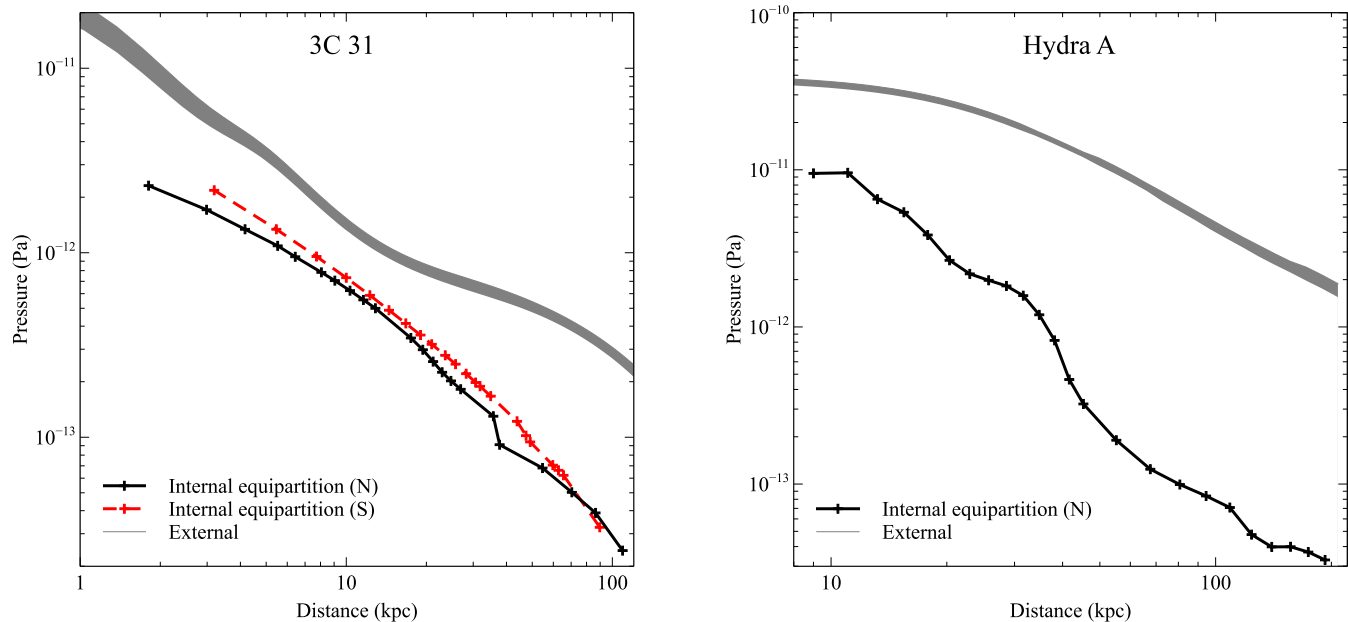


**Figure 1.** External and internal (equipartition) pressure profiles for the two sources 3C 31 (l) and Hydra A (r). The external pressures derived from X-ray measurements are shown as shaded regions, which indicate the  $1\sigma$  errors, and the internal, equipartition pressures with the assumption of no protons are given by the solid black (3C31 north, Hydra A north) and dashed red (3C31 south) lines. The statistical uncertainties on the internal pressures are negligible compared to model assumptions and so are not plotted.

$\sim 10$  kpc. This figure illustrates clearly that on scales  $> 10$  kpc the contribution of the radiating material to the total internal pressure of the radio source, in the equipartition case, must decrease substantially as the jet evolves out into the group or cluster environment. Alternatively, if equipartition between radiating particles and magnetic field does not hold, then there must be a systematic departure from this condition that increases with distance from the nucleus and group/cluster centre. Such an effect was first observed in ROSAT environmental studies (e.g. Hardcastle et al. 1998; Worrall & Birkinshaw 2000), and is also seen in our combined *Chandra* and *XMM-Newton* analysis of NGC 6251 (Evans et al. 2005) and 3C 465 (Hardcastle et al. 2005); however, the higher quality of the X-ray and radio pressure constraints in the new work we present here places the result on a much firmer footing.

We have considered in detail the possible effects of projection on this conclusion (see Section 3.4). Neither 3C 31 or Hydra A is thought to be highly projected, and for plausible jet orientations the plots in Fig. 1 and 2 do not alter significantly as the two effects of projection act in the same direction: the internal pressure decreases with  $\theta_{los}$  since the jet volume at a given projected distance increases, and the external pressure acting on the jet at this projected distance decreases because it is further out in the X-ray atmosphere whose pressure is dropping off.

Although such detailed pressure profile comparisons have not been carried out previously, it is interesting to note that a similar behaviour can be seen at a statistical level in the sample of cluster cavities studied by Dunn et al. (2005), where the so-called “ghost” cavities are typically at much larger distances from the cluster centre than the active lobes, which are systematically closer to pressure balance assuming  $\kappa = 0$ .

The pressure constraints shown in Fig. 2 can be used to test a range of models that have been proposed for the particle or field content dominating the energy budget of low-power radio lobes.

In the following section we consider four models for the dominant energy content of the lobes:

- **Model I – lepton dominance:** the jets and lobes are out of equipartition, but the contribution from protons remains negligible and it is the radiating electrons and positrons that dominate the internal pressure
- **Model II – magnetic field dominance:** the jets and lobes are out of equipartition, but the contribution from protons remains negligible and the magnetic field dominates the internal pressure.
- **Model III – relativistic proton or ion dominance:** the jets and lobes are in equipartition, with relativistic protons (and/or ions) dominating the internal pressure (i.e.  $\kappa \gg 0$ )
- **Model IV – thermal gas dominance (entrainment):** the jets and lobes are in equipartition, with thermal material, likely entrained from the surrounding intragroup medium, dominating the internal pressure (i.e.  $\kappa \gg 0$ )

It is clear that more complex models are possible – in particular, it is plausible that non-radiating particles are present, but the jets and lobes are not at equipartition in all locations along the jet. Such models are harder to test, and so we begin by considering the four simpler models listed above.

### 3.1 Departures from equipartition (Models I and II)

As previously stated, it is clear from Figs 1 and 2 that in order for a departure from equipartition to be the explanation for the apparent “missing” pressure in FRI lobes, the jets must evolve further and further from the equipartition condition as the source expands (apart from in the very inner parts – we will consider the implications of the differing behaviour in the inner  $\sim 10$  kpc of 3C 31 in Section 3.6)

The energy densities and magnetic field strengths required in order that the total energy density in the synchrotron-emitting

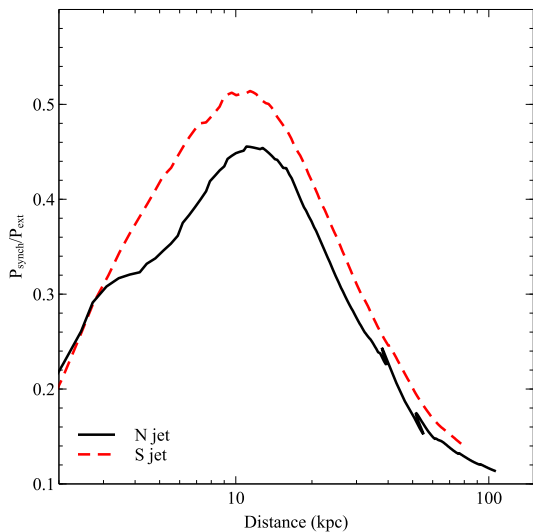


**Figure 2.** The fraction of required internal pressure that can be provided by the synchrotron-emitting components of the jets if at equipartition, as a function of distance from group/cluster centre for 3C 31, showing that this component can provide a decreasing fraction of the jet pressure on scales of tens to hundreds of kpc. Line styles are as for Fig. 1.

plasma should match the measured external pressure were determined by modelling the electron energy distribution using the parameters discussed in Section 2.2. Fig. 3 shows the evolution of the required energy ratio between magnetic fields and leptons required to maintain pressure balance with the surrounding hot gas for Models I and II.

In Model I (lepton domination) the particle energy dominates by a factor  $\sim 100$  in the inner regions, then, after an initial decrease, increases to  $\sim 500$  at hundred-kpc distances. For the large electron densities required in this model, the predicted level of X-ray inverse-Compton radiation from the radio jets and lobes would be significant, and can be ruled out in a number of individual cases (e.g. Croston et al. 2003; Hardcastle & Croston 2010). In particular, Hardcastle & Croston (2010) have examined in detail the constraints on inverse Compton emission from Hydra A, and conclude that relativistic electrons (and positrons) can contribute at most  $\sim 6$  per cent of the internal pressure of the radio lobes. We can therefore conclusively rule out this explanation. For 3C 31, we considered the outermost region of our profile, and calculated the predicted level of X-ray inverse Compton emission at 1 keV using the SYNCH code of Hardcastle et al. (1998) under the assumptions of Model I. We find that the observed residual level of X-ray flux in this region after background subtraction is a factor  $\sim 2000$  times lower than the prediction of this model, consistent with results for other FRI sources.

In Model II (magnetic field domination), the energy ratio  $U_B/U_E$  evolves similarly to Model I, with the factor by which the magnetic field dominates increasing from around 30 to  $\sim 100$  by hundred kpc scale distances. Fig. 4 shows the magnetic field strengths required as a function of distance to achieve pressure balance in this model. The magnetic field strengths required are high ( $\sim 10 - 40 \mu\text{G}$ ), decreasing by a factor of a few from the inner parts to hundred kpc scale distances. This model requires the generation of magnetic field energy density along the source. The dashed and dotted lines in Fig. 4 show the expected evolution of magnetic field strength due to adiabatic expansion for the case of a predominantly

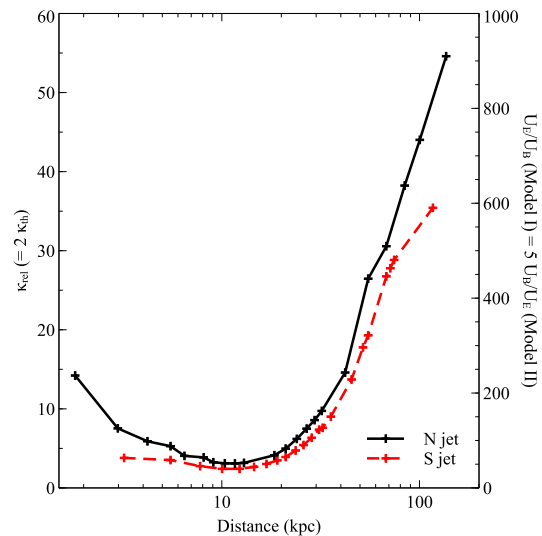


**Figure 3.** The evolution of the energetically dominant component of the 3C 31 jets with distance, showing the ratio of lepton to magnetic field energy density for Model I, the inverse ratio for Model II, and the proton/ion content  $\kappa$  for Models III and IV. Line styles are as for Fig. 1.

radial/toroidal and predominantly longitudinal field structure, respectively (e.g. Baum et al. 1997). A constant velocity profile was assumed, which is conservative, as a decreasing velocity would steepen the losses for the perpendicular components of  $B$ . Hence a passively evolving magnetic field component is inconsistent with the observations. The results shown in Fig. 4 are not consistent with previously proposed models for cylindrical jets with helical  $B$  fields (e.g. Nakamura et al. 2006), but such models are also inconsistent with FRI jet geometries and polarization structures (e.g. Laing 1981; Laing et al. 2008). The requirement for a slow decrease in  $B$  along the jets (despite lateral expansion of the jet) could be consistent with a model in which turbulence increasingly amplifies the magnetic field on large scales; however, this would need to take place with no appreciable particle acceleration for consistency with the radio constraints, and turbulent amplification of magnetic fields beyond equipartition values is challenging (De Young 1980). Our results show that energy would have to be being transferred from the particle population to the magnetic field to a greater and greater extent at larger distances. This model cannot be ruled out directly, but from the constraints on the model given above we conclude that magnetic domination of the jets and lobes is highly unlikely.

### 3.2 Contributions from non-radiating particles (Models III and IV)

The question of whether or not the inner jets of radio galaxies consist of an electron-positron or electron-proton plasma is a long-standing one, which has not yet been resolved satisfactorily, despite substantial efforts over the past couple of decades (e.g. Ghisellini et al. 1992; Celotti & Fabian 1993; Wardle et al. 1998; Homan et al. 2009). On kpc scales, there is an obvious additional source of non-radiating particles in the form of material entrained into the jets from the surroundings: there is substantial evidence for entrainment in FRI jets, and the standard picture of FRI dynamics relies on entrainment to decelerate the jets from relativistic to transonic speeds on scales of a few kpc (e.g. Bicknell 1994; Laing & Bri-

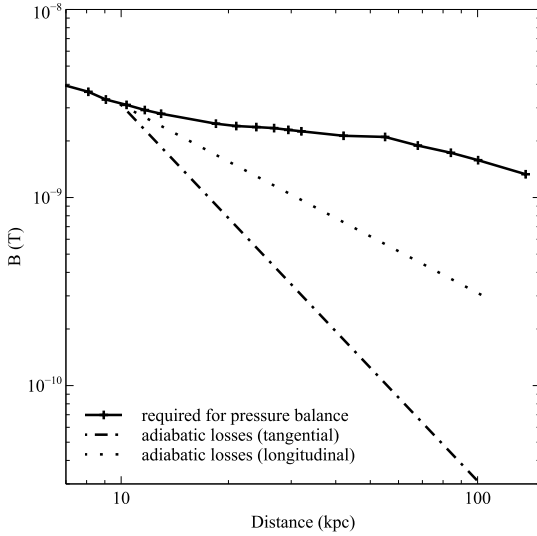


**Figure 4.** The magnetic field strength required as a function of distance in the case where magnetic field energy dominates the internal pressure (shown for the northern jet of 3C 31). The dotted and dashed lines show the expected evolution of magnetic field strength due to adiabatic expansion for the case of a predominantly tangential and predominantly longitudinal field structure, respectively. Line styles are as for Fig. 1.

dle 2002). In this section we consider models in which relativistic protons (and/or ions (Model III) or thermal gas entrained from the surroundings (Model IV) dominate the internal pressure.

The contribution from heavy particles (protons/ions) required to achieve pressure balance can be determined straightforwardly under the assumption of equipartition of energy between all particles (radiating and non-radiating) and magnetic field. Details of this calculation for the cases of relativistic and thermal gas are provided in Appendix A. In Fig. 3 we plot the required ratio of energy density in non-radiating particles to radiating particles for these two models.

Fig. 5 shows the run of energy density in relativistic protons (or ions) required to balance the external pressure for Model III, assuming equipartition of particles (both radiating and non-radiating) with magnetic field. If the electron population suffers significant radiative losses (which do not affect the proton/ion energy density), it might be expected that the relative energy density in protons (and/or ions) would increase with distance, as required by the external pressure data. However, if the energy is carried by relativistic protons injected in the jets' inner regions, then their energy density would be expected to evolve adiabatically with distance, in the absence of significant radiative losses or particle acceleration. Fig. 5 shows that the simplest version of Model III in which protons are injected only in the inner jet is not viable, because the proton energy density in this model decreases much less steeply with distance than expected as a result of adiabatic losses (calculated from 10 kpc outwards). We can therefore rule out a model in which protons injected in the inner regions evolve passively along the jet. For relativistic protons and/or ions to dominate the jets and lobes over their entire length, significant particle acceleration is required on scales of tens to hundreds of kpc (which must not significantly affect the lepton population).

A model in which entrainment of surrounding material leads to an increasing thermal gas content as the jets evolve (whether or not they initially contain relativistic protons), such as Model IV, is

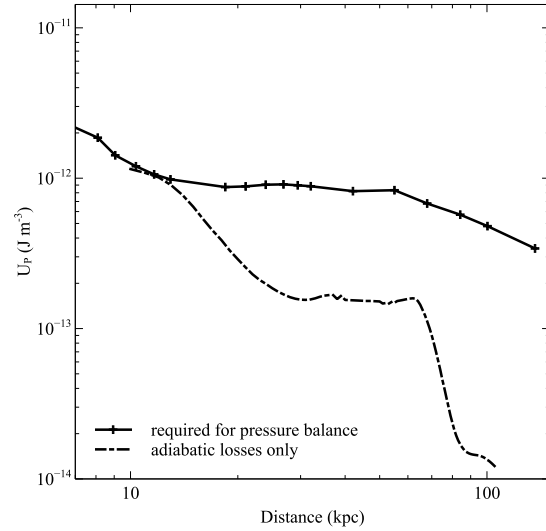


**Figure 5.** The energy density in relativistic protons and/or ions required to balance the external pressure (filled squares), shown for the northern jet of 3C 31. The dashed and dotted lines indicate the expected evolution of energy density with distance along the source assuming adiabatic losses. Note that the flattening of the adiabatic model between 20 and 70 kpc is caused by the jet's cylindrical geometry in that region (see also Fig. 6)

more consistent with the data as it provides a simple explanation for the decreasing energetic importance of the radiating particles as the jet evolves. Fig. 3 shows how the ratio of energy density in non-radiating particles to radiating particles must evolve along the jet in this model. This evolution of energy density could occur either by increasing entrainment (via an increasingly large boundary layer), or by increased heating/acceleration of entrained thermal gas. The required entrainment rate for Model IV can be obtained by consideration of mass, momentum and energy flux conservation along the jet. In the following section we develop a toy model to investigate this scenario.

### 3.3 An entrainment model on for 3C 31

We model the region of jet between 12 kpc and 140 kpc, which is where the X-ray constraints are tight while the uncertainties on jet geometry are acceptable (beyond this distance further jet bends and flaring making it difficult to constrain the geometry). The inner boundary is chosen to be beyond the initial deceleration region according to the model of Laing & Bridle (2002), so that relativistic effects can be neglected. We assume Model IV, above, i.e. the following assumptions hold: (1) the jet internal pressure,  $P_{int}$ , balances the external pressure ( $P_{ext}$ , as measured from the X-ray observations) at each radius; (2) the internal pressure has contributions from magnetic field ( $P_B$ ), synchrotron radiating leptons ( $P_E$ ), and thermal gas entrained from the environment ( $P_{th}$ ); and (3) the magnetic field strength and energy density are assumed to be in equipartition with the total particle energy density (from synchrotron-radiating and non-radiating particles). We later discuss the effects of relaxing the final assumption.

By making use of the (non-relativistic) equations for conservation of momentum and energy flux along the jet, the density and temperature of the 'missing' thermal component of the jet can be obtained, as described in detail in Appendix B. We require initial conditions of density and velocity at the inner boundary. We take

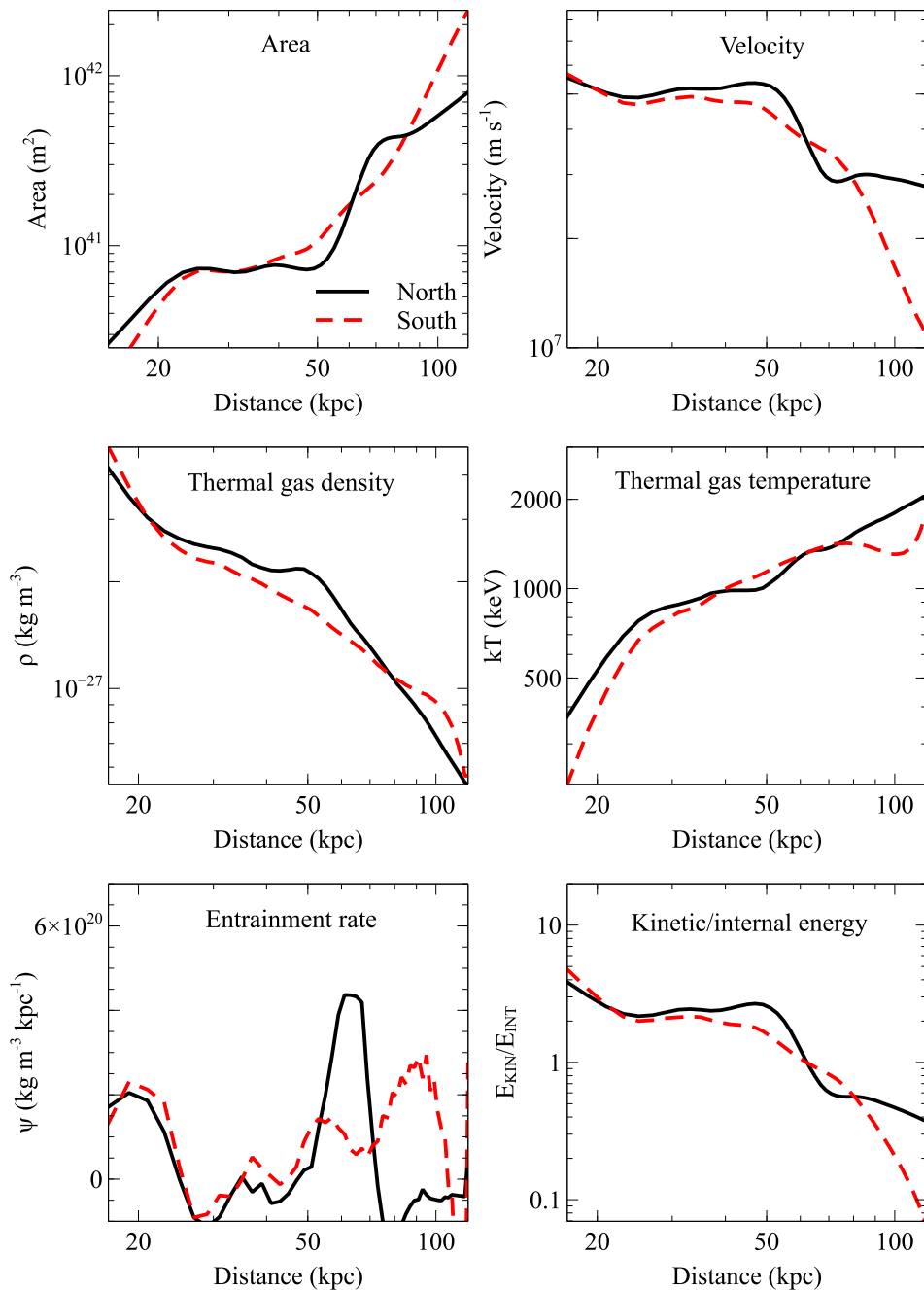


**Figure 6.** Jet properties vs. distance for our entrainment model, assuming an initial temperature for the thermal component of 100 keV. Top row: cross-sectional area (l) and velocity (r), middle row: gas density (l) and temperature (r) for the thermal component, bottom row: mass entrained per unit length (l) and ratio of kinetic to jet internal energy flux (r), all shown for the northern (black solid) and southern (red dashed) jets of 3C 31.

the jet velocity of 3C 31 at 12 kpc from the model of Laing & Bridle (2002) as our inner boundary condition, and assume a range of initial gas temperatures. The choice of temperature for the thermal component at 12 kpc sets a boundary condition on the gas density (via the pressure constraints), and hence determines the jet power. As discussed later, we can therefore use the jet power as a consistency check on the most appropriate choice of initial temperature.

Fig. 6 shows some illustrative results, with initial conditions chosen to obtain jet powers matched for the two jets, and in broad

agreement with the model of Laing & Bridle (2002) (this requires initial temperatures at 12 kpc of 100 keV and 230 keV for the northern and southern jets, respectively). In this model the behaviour of the two jets is broadly similar, but with some differences driven by variation in how the jet geometry evolves. The northern jet can be divided into several regions on scales of tens to hundreds of kpc in which its geometry differs. As shown in the top left panel of the figure, the cross-sectional area initially increases steeply with distance, the jet then becomes cylindrical between around 20 kpc to

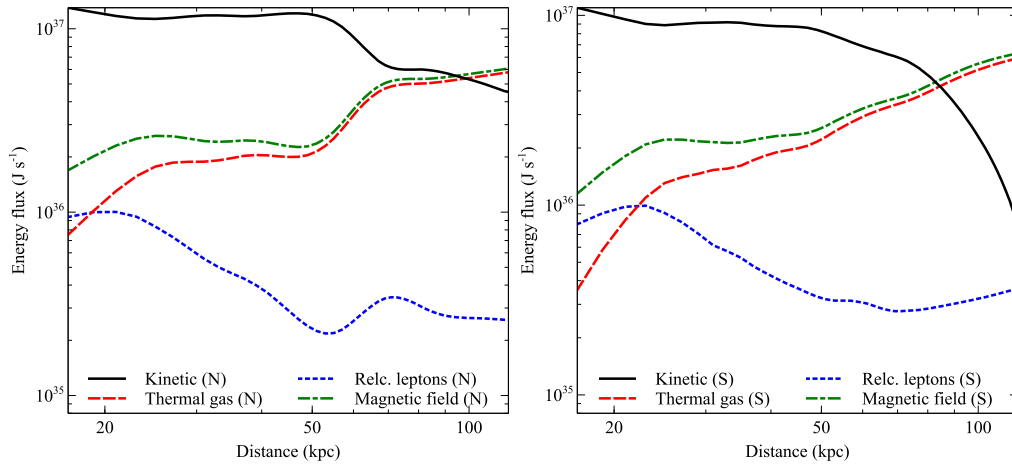


**Figure 7.** The evolution of energy flux with distance along the jet, for models with matched jet power, showing kinetic energy (black), magnetic field energy (green), internal energy of thermal particles (red) and of relativistic leptons (blue), with left and right panels indicating the northern and southern jets, respectively.

60 kpc; and then the jet radius increases again to 100 kpc scales and beyond. These geometrical features show an interesting correspondence with bends in the jet (occurring at both of those transition points), and with the external pressure gradient, as the pressure profile flattens at around 20 kpc (plausibly moving from a galaxy-scale halo to a group-scale atmosphere) and then steepens again between 50 and 100 kpc. The density profile that results from an assumption of constant temperature along the jet shows features that correspond to this geometry, with an inner region of increasing density, followed by a region of constant density and then a decreasing density in the outer region as the jet/plume widens. Finally the bottom left panel shows that in this model the entrainment must be fairly localized, with large amounts of material ingested at the two transition points of  $\sim 20$  and 60 kpc (note that these are distances along the jet centre-line, rather than radial distances in the group atmosphere). At other times the entrainment rate is low. The southern jet expands more smoothly, and somewhat faster, consequently requiring entrainment to be spread out over larger distances. At large distances the cross-sectional area expands significantly more steeply than for the northern jet, which leads to higher entrainment, deceleration, and thermalization of kinetic energy.

The conservation-law analysis of Laing & Bridle (2002) leads to an entrainment rate at 12 kpc of  $\sim 10^{20} \text{ kg s}^{-1} \text{ kpc}^{-1}$ . The models shown in Fig 6 are consistent with this level of entrainment; however, it is also possible that the entrainment in our model results from fairly localised disruption of the jet at its bends, which may be unconnected to the steadier entrainment implied by the model of Laing & Bridle (2002), in which case consistency with their measurement of entrainment rate is not required.

In our model the energy flux is primarily in the form of kinetic energy in the inner parts of the jet, but is increasingly converted into internal energy of the thermal (and presumably relativistic) particles, as shown in Fig 7. The temperatures required by our model, for realistic jet powers, are much higher than the temperature of the surrounding gas, indicated that the entrained material must be heated fairly rapidly by tapping the jet’s kinetic energy. We are assuming that all of the thermal material at a particular distance in the jet has a single temperature, which is simplistic; however, at

any given position the majority of material will have been in the jet for some time with recently entrained gas comprising only a small fraction. We note that temperatures of  $> 100 \text{ keV}$  for entrained gas are consistent with the limits on the presence of thermal material in cluster cavities obtained from limits on the thermal X-ray emission due to this gas (e.g. Blanton et al. 2003; Sanders & Fabian 2007). The ‘thermal’ component, although very hot, remains (predominantly) sub-relativistic in this model, although a non-thermal, relativistic tail cannot be ruled out.

Hence we conclude that our simple entrainment model is qualitatively consistent with providing the dominant energetic contribution to the jets and plumes of 3C 31 on scales from 10 to 100 kpc. Most interestingly, if entrainment does drive the source energetics, then much of the mass ingestion appears to be localised, and coincide with regions where the jets bend and/or spread. In particular, the two regions of the northern jet where entrainment takes place in our model coincide with the flattening and steepening of the external pressure profile, it is clear that the gas distribution in the group environment determines the energetic evolution of the radio-galaxy plasma on these scales.

Our assumption of equipartition of energy density between particles and magnetic field may not be correct. We argue in Section 3.1 that non-equipartition models with no protons are unlikely to be correct, but a model where thermal and relativistic particles together dominate the energetics, with a lower magnetic field energy density, cannot be ruled out. However, such a model would not strongly differ in the qualitative picture for the evolution of thermal content of the jet – the radio synchrotron constraints mean that if the magnetic field strength contributes a lower fraction of the internal energy flux then the electron contribution must increase. Significant entrainment would still be required at the locations seen in Fig 6, but the quantities of mass entrained and the required temperature profile could be somewhat different.

### 3.4 Geometrical uncertainties

Uncertainty in the geometry of the radio jets, and in particular how the jet orientation changes relative to the plane of the sky at the ob-



served jet bends, is potentially a major limitation of our analysis. As discussed in Section 3, our main observational result – that the synchrotron-emitting components of the jet contribute a decreasing fraction of the jet pressure, if at equipartition – is not affected by uncertainties in projection. In a geometry with high inclination, the resulting larger synchrotron emitting volume and lower external pressure acting on a particular region due to larger radial distance in the cluster counteract each other, which means that the overall result is largely unaffected. The evolution of the non-radiating particle energy fraction in Models III and IV (or of  $U_E$  and  $U_B$  in Models I and II) are therefore qualitatively similar in any plausible geometry, even though the numerical values will change somewhat. We do not attempt here to derive precise constraints on the jet energy content at a particular radius, but rather to develop a robust qualitative understanding of how the components of the jet plasma evolve. Therefore, while we acknowledge that the geometry is poorly constrained, our general conclusions are robust.

### 3.5 Uncertainties due to assumption electron energy distribution

A further uncertainty comes from our lack of knowledge of the low-energy electron distribution as a function of distance along the jets. This will soon be remedied by ongoing work with LOFAR (Heesen et al., in prep); however, at present we can only extrapolate to the lowest frequencies from the radio spectrum at 330 MHz. As discussed in Section 2.2 we assumed a low-frequency spectral index of  $\alpha = 0.55$  (e.g. Laing & Bridle 2013) and a value of  $\gamma_{min} = 10$ . Evidence for  $\gamma_{min} \gg 1$  comes from the broad-band spectra of hotspots (e.g. Meisenheimer et al. 1997; Carilli et al. 1999); however, the situation in FRI jets remains unknown. For the electron distribution assumptions to significantly alter our results we would require an evolution in the low-frequency properties of the jet with distance from the nucleus. If  $\gamma_{min}$  is determined by the particle acceleration process that occurs in the inner jet, then it is plausible that it could evolve to lower energies (e.g. via adiabatic losses) at the plasma is advected downstream. Alternatively, the low-frequency spectral index could evolve to become steeper at larger distances, but there is no indication that this is the case in the existing 330-MHz data (e.g. the spectral index between 330 MHz and 608 MHz is  $\sim 0.58$  for the outermost region we consider in the northern jet).

We investigated the electron energy distribution that would be required to achieve pressure balance in the outermost region of the 3C 31 northern plume, assuming equipartition (the non-equipartition cases having been considered previously). Simply reducing  $\gamma_{min}$  to 1, while extrapolating from the observed spectral index of 0.55, is inadequate to achieve pressure balance. It would be necessary for the radio spectrum to steepen significantly below 330 MHz, to  $\alpha > 0.9$ , and to have a low-energy cut-off of  $\gamma_{min} = 1$  in order for the synchrotron emitting components to provide all of the pressure within the lobes at this distance. As the radiation from such a component is currently unobservable with existing radio data, this scenario is effectively indistinguishable from Models III and IV, above; however, it is difficult to reconcile with particle acceleration models, and would require a second relativistic particle population that has previously been undetected. Such a dominant lepton population with  $\gamma < 1500$ , emitting below 330-MHz, cannot currently be ruled out by existing radio or X-ray inverse Compton constraints. We also cannot at this stage rule out more complex models in which the spectral index (and  $\gamma_{min}$ ) vary while the contribution from thermal gas also changes with distance, but

we look forward to being able to test such models in the near future with LOFAR data.

### 3.6 Evolution in the inner jet region

We have focused mainly on the region of the jet beyond 10 kpc, where it is thought to be subrelativistic and evolving into the group gas environment. As shown in Figs. 1 and 2, the evolution of the jet plasma appears to be different in the region inside 10 kpc. We have made no attempt to correct for the effects of relativistic beaming in calculating our radio emissivity profile as our focus is on the outer regions, but the effect of “de-beaming” the synchrotron emissivity [assuming the velocity model of Laing & Bridle (2002)] is a small decrease in the pressure of the synchrotron components of the northern jet, and an increase in their contribution for the southern jet. Hence this does not qualitatively alter the behaviour of the northern jet, though it brings the southern jet to have a roughly constant ratio of  $P_{ext}/P_{synch}$  in the inner region.

If Model IV above is the correct explanation for the evolution of the jet plasma on scales beyond 10 kpc, then other effects must be more important in the inner region. One possibility is that the jet is initially significantly electron (or relativistic electron and proton) dominated (e.g. due to substantial particle acceleration in the inner jet) before evolving towards equipartition between particles and magnetic field, with entrainment taking over as an important mechanism affecting the overall energetics from around 10 kpc. Such a model is somewhat speculative, however, with the microphysics of energy transfer between jet components poorly understood and difficult to test.

## 4 CONCLUSIONS

We have shown that X-ray and radio measurements of external pressure and internal pressure from radiating material as a function of distance along the source can be used to distinguish between models for the contents of radio lobes. Considering in detail the cases of 3C 31 and Hydra A, we have shown that:

- The fractional contribution to the total energy budget from synchrotron-emitting components (relativistic leptons and magnetic field), if at equipartition, must decrease with distance from the central AGN.
- A model in which the energetics are dominated by relativistic leptons can be ruled out by inverse-Compton limits.
- Magnetic domination requires the magnetic field strength to remain close to constant along the jet, which is implausible given the jet geometry, due to the need to convert an increasing fraction of the jet energy into magnetic field as the jet evolves, without producing significant particle acceleration.
- A model in which relativistic protons/ions injected in the inner jet dominate the jet energetics and evolve adiabatically along the jet is ruled out.
- Finally we have demonstrated that a simple entrainment model is consistent with the external pressure constraints and the evolution of radio emissivity, with regions of entrainment corresponding to locations of jet bending/disruption and changes in the external pressure profile. Such a model requires a high temperature for the entrained component, and an increasing temperature with distance, consistent with a rapidly decreasing kinetic energy flux of the jet being converted to particle and magnetic field internal energies.

The results presented here are based on consideration of a single object, for which the highest quality radio and X-ray data on the scales of interest are available. Our detailed pressure comparison for Hydra A, as well as indications from less well constrained comparisons for other objects (Evans et al. 2005; Hardcastle et al. 1998; Worrall & Birkinshaw 2000) and circumstantial evidence from observations of cluster cavities, mean that it is plausible that our conclusion that an entrainment-dominated model is favoured in 3C 31 can be generalised to low-power radio galaxies in general. In future work we will apply these analysis methods to other systems with high-quality X-ray and radio data, as well as incorporating new low-frequency radio measurements to minimise uncertainties from extrapolation of the electron energy distribution.

## ACKNOWLEDGMENTS

JHC acknowledges support from the South-East Physics Network (SEPNet) and from the Science and Technology Facilities Council (STFC) under grant ST/J001600/1. We would like to thank Robert Laing for providing the 1.4-GHz map of 3C 31. We would also like to thank the referee, Geoff Bicknell, for a helpful report, which has enabled us to improve the paper.

## REFERENCES

- Baum S. A., O’Dea C. P., Giovannini G., Biretta J., Cotton W. B., de Koff S., Feretti L., Golombek D., Lara L., Macchetto F. D., Miley G. K., Sparks W. B., Venturi T., Komissarov S. S., 1997, *ApJ*, 483, 178
- Bicknell G. V., 1994, *ApJ*, 422, 542
- Birzan L., McNamara B. R., Nulsen P. E. J., Carilli C. L., Wise M. W., 2008, *ApJ*, 686, 859
- Blanton E. L., Sarazin C. L., McNamara B. R., 2003, *ApJ*, 585, 227
- Burbidge G. R., 1956, *ApJ*, 124, 416
- Carilli C. L., Kurk J. D., van der Werf P. P., Perley R. A., Miley G. K., 1999, *AJ*, 118, 2581
- Celotti A., Fabian A. C., 1993, *MNRAS*, 264, 228
- Croston J. H., Hardcastle M. J., Birkinshaw M., 2005, *MNRAS*, 357, 279
- Croston J. H., Hardcastle M. J., Birkinshaw M., Worrall D. M., 2003, *MNRAS*, 346, 1041
- Croston J. H., Hardcastle M. J., Birkinshaw M., Worrall D. M., Laing R. A., 2008, *MNRAS*, 386, 1709
- David L. P., Nulsen P. E. J., McNamara B. R., Forman W., Jones C., Ponman T., Robertson B., Wise M., 2001, *ApJ*, 557, 546
- De Young D. S., 1980, *ApJ*, 241, 81
- De Young D. S., 2006, *ApJ*, 648, 200
- Dunn R. J. H., Fabian A. C., 2004, *MNRAS*, 355, 862
- Dunn R. J. H., Fabian A. C., Celotti A., 2006, *MNRAS*, 372, 1741
- Dunn R. J. H., Fabian A. C., Taylor G. B., 2005, *MNRAS*, 364, 1343
- Evans D. A., Hardcastle M. J., Croston J. H., Worrall D. M., Birkinshaw M., 2005, *MNRAS*, 359, 363
- Fabian A. C., 2012, *ARA&A*, 50, 455
- Fanaroff B. L., Riley J. M., 1974, *MNRAS*, 167, 31P
- Ghisellini G., Celotti A., George I. M., Fabian A. C., 1992, *MNRAS*, 258, 776
- Hardcastle M. J., Birkinshaw M., Cameron R. A., Harris D. E., Looney L. W., Worrall D. M., 2002, *ApJ*, 581, 948
- Hardcastle M. J., Birkinshaw M., Worrall D. M., 1998, *MNRAS*, 294, 615
- Hardcastle M. J., Croston J. H., 2010, *MNRAS*, 404, 2018
- Hardcastle M. J., Croston J. H., Kraft R. P., 2007, *ApJ*, 669, 893
- Hardcastle M. J., Sakelliou I., Worrall D. M., 2005, *MNRAS*, 359, 1007
- Hardcastle M. J., Worrall D. M., Birkinshaw M., 1998, *MNRAS*, 296, 1098
- Hardcastle M. J., Worrall D. M., Kraft R. P., Forman W. R., Jones C., Murray S. S., 2003, *ApJ*, 593, 169
- Homan D. C., Lister M. L., Aller H. D., Aller M. F., Wardle J. F. C., 2009, *ApJ*, 696, 328
- Ineson J., Croston J. H., Hardcastle M. J., Kraft R. P., Evans D. A., Jarvis M., 2013, *ApJ*, 770, 136
- Isobe N., Tashiro M., Makishima K., Iyamoto N., Suzuki M., Murakami M. M., Mori M., Abe K., 2002, *ApJ*, 580, L111
- Kataoka J., Stawarz L., 2005, *ApJ*, 622, 797
- Laing R. A., 1981, *ApJ*, 248, 87
- Laing R. A., Bridle A. H., 2002, *MNRAS*, 336, 1161
- Laing R. A., Bridle A. H., 2004, *MNRAS*, 348, 1459
- Laing R. A., Bridle A. H., 2013, *MNRAS*, 432, 1114
- Laing R. A., Bridle A. H., Parma P., Feretti L., Giovannini G., Murgia M., Perley R. A., 2008, *MNRAS*, 386, 657
- Laing R. A., Canvin J. R., Bridle A. H., Hardcastle M. J., 2006, *MNRAS*, 372, 510
- Li H., Lapenta G., Finn J. M., Li S., Colgate S. A., 2006, *ApJ*, 643, 92
- Longair M. S., 1994, *High energy astrophysics. Vol.2: Stars, the galaxy and the interstellar medium*
- McNamara B. R., Nulsen P. E. J., 2007, *ARA&A*, 45, 117
- Meisenheimer K., Yates M. G., Roeser H.-J., 1997, *A&A*, 325, 57
- Morganti R., Fanti R., Gioia I. M., Harris D. E., Parma P., de Ruiter H., 1988, *A&A*, 189, 11
- Nakamura M., Li H., Li S., 2006, *ApJ*, 652, 1059
- Sanders J. S., Fabian A. C., 2007, *MNRAS*, 381, 1381
- Taylor G. B., Perley R. A., Inoue M., Kato T., Tabara H., Aizu K., 1990, *ApJ*, 360, 41
- Wardle J. F. C., Homan D. C., Ojha R., Roberts D. H., 1998, *Nature*, 395, 457
- Wise M. W., McNamara B. R., Nulsen P. E. J., Houck J. C., David L. P., 2007, *ApJ*, 659, 1153
- Worrall D. M., Birkinshaw M., 2000, *ApJ*, 530, 719

## APPENDIX A. METHOD FOR CALCULATING $\kappa$ (RATIO OF NON-RADIATING PARTICLES TO RELATIVISTIC LEPTON ENERGY DENSITY)

We assume:

- The jet internal pressure,  $P_{int}$ , balances the external pressure at each distance,  $P_{ext}$ , which is measured from the X-ray observations.
- The internal pressure has contributions from magnetic field,  $P_B$ , synchrotron-radiating relativistic particles,  $P_E$ , and thermal gas entrained from the environment,  $P_{th}$ .
- Pressure balance along the jet is described by the following relation between the external pressure and the internal energy densities of magnetic field, relativistic and non-relativistic (thermal) particles:

$$P_{ext} = \frac{1}{3}U_E + \frac{1}{3}U_B + fU_P \quad (1)$$

where  $f$  is  $1/3$  for relativistic protons/ions and  $f = 2/3$  for thermal gas.

The ratio of energy densities in non-radiating particles and synchrotron-emitting particles (relativistic leptons) is  $\kappa$ , i.e.  $U_P = \kappa U_E$ , leading to the following equations for the relativistic case:

$$3P_{ext} = (1 + \kappa_{rel})U_E + U_B \quad (2)$$

and the thermal case:

$$3P_{ext} = (2\kappa_{th} + 1)U_E + U_B \quad (3)$$

If we assume that the distribution of electron energy density is described by a power law with index  $p \neq 2$  (i.e.  $N(E) = N_0 E^{-p}$ ), then the electron energy density is given by:

$$U_E = \int_{E_{min}}^{E_{max}} EN(E)dE = N_0 \frac{E_{max}^{2-p} - E_{min}^{2-p}}{2-p} \quad (4)$$

where  $N_0$  is the electron energy density normalization,  $p$  is the electron energy index,  $E_{min}$  and  $E_{max}$  are the lower and upper cut-offs of the electron energy distribution.

We assume equipartition between magnetic field and all particles (relativistic and non-relativistic), i.e.  $U_B = (1 + \kappa)U_E$ , which leads to the standard expression for the equipartition magnetic field strength:

$$B_{eq} = \left[ \frac{2\mu_0(1 + \kappa)J(\nu)\nu^{\frac{(p-1)}{2}}}{c_1(2-p)} (E_{max}^{2-p} - E_{min}^{2-p}) \right]^{\frac{2}{p+5}} \quad (5)$$

where  $J(\nu)$  is the synchrotron emissivity at a frequency  $\nu$ , given by

$$J(\nu) = c_1 N_0 \nu^{-\frac{(p-1)}{2}} B^{\frac{(p+1)}{2}} \quad (6)$$

where  $c_1$  is a constant (Longair 1994):

$$c_1 = k(p) \frac{e^3}{\epsilon_0 c m_e} \left( \frac{m_e^3 c^4}{e} \right)^{-\frac{(p-1)}{2}} \quad (7)$$

where  $k(p)$  is 0.050407 for  $p = 2$ , 0.039484 for  $p = 2.2$ , and 0.031547 for  $p = 2.4$ . We can now make use of the pressure constraints derived earlier for the relativistic proton/ion and thermal gas cases (Eqs. 2 and 3, applying to Models III and IV, respectively) to get a second expression for  $B$ . For Model III, substituting in for  $U_E$  in Eq. 2 gives:

$$\frac{B^2}{2\mu_0} = 3P_{ext} - \frac{(1 + \kappa)N_0}{2-p} [E_{max}^{2-p} - E_{min}^{2-p}] \quad (8)$$

and substituting in Eq. 6 gives:

$$\frac{B^2}{2\mu_0} = 3P_{ext} - \frac{(1 + \kappa)J(\nu)\nu^{\frac{(p-1)}{2}} B^{-\frac{(p+1)}{2}}}{c_1(2-p)} [E_{max}^{2-p} - E_{min}^{2-p}] \quad (9)$$

We can now substitute in our previously derived expression for the equipartition  $B$  field (Eq. 5):

$$\left[ \frac{2\mu_0(1 + \kappa_{rel})J(\nu)\nu^{\frac{(p-1)}{2}}}{c_1(2-p)} (E_{max}^{2-p} - E_{min}^{2-p}) \right]^{\frac{4}{p+5}} (2\mu_0)^{-1} = 3P_{ext} - \frac{(1 + \kappa_{rel})J(\nu)\nu^{\frac{(p-1)}{2}}}{c_1(2-p)} [E_{max}^{2-p} - E_{min}^{2-p}] \left[ \frac{2\mu_0(1 + \kappa_{rel})J(\nu)\nu^{\frac{(p-1)}{2}}}{c_1(2-p)} (E_{max}^{2-p} - E_{min}^{2-p}) \right]^{-\frac{(p+1)}{(p+5)}} \quad (10)$$

This expression can be simplified to:

$$\kappa_{rel} = \left( \frac{3P_{ext}}{2} \right)^{\frac{p+5}{4}} (2\mu_0)^{\frac{p+1}{4}} c_2^{-1} \quad (11)$$

where

$$c_2 = \frac{J(\nu)\nu^{\frac{p-1}{2}}}{c_1(2-p)} [E_{max}^{2-p} - E_{min}^{2-p}] \quad (12)$$

For the thermal case (Model IV), a similar expression can be derived from Eq 3, with a slightly difference dependence on  $\kappa$ :

$$\left[ \frac{2\mu_0(1 + \kappa_{th})J(\nu)\nu^{\frac{(p-1)}{2}}}{c_1(2-p)} (E_{max}^{2-p} - E_{min}^{2-p}) \right]^{\frac{4}{p+5}} (2\mu_0)^{-1} = 3P_{ext} - \frac{(1 + \kappa_{th})J(\nu)\nu^{\frac{(p-1)}{2}}}{c_1(2-p)} [E_{max}^{2-p} - E_{min}^{2-p}] \left[ \frac{2\mu_0(1 + \kappa_{th})J(\nu)\nu^{\frac{(p-1)}{2}}}{c_1(2-p)} (E_{max}^{2-p} - E_{min}^{2-p}) \right]^{-\frac{(p+1)}{(p+5)}} \quad (13)$$

which simplifies to:

$$3P_{ext} = (2\mu_0)^{-\frac{p+1}{p+5}} c_2^{\frac{4}{p+5}} \left[ (1 + \kappa_{th})^{\frac{4}{p+5}} + (2\kappa_{th} + 1)(1 + \kappa_{th})^{-\frac{p+1}{p+5}} \right] \quad (14)$$

For both models we have now have an equation that contains only one unknown,  $\kappa$ . For an observed  $S(\nu)$  and  $P_{ext}$ , the value of  $\kappa$  can therefore be obtained (numerically, in the thermal case), which also allows  $B$ ,  $U_E$ , and  $U_p$ , and finally the thermal gas density in the jet for a given assumed temperature, to be obtained.

## APPENDIX B. DETAILS OF ENTRAINMENT CALCULATIONS

For a steady-state jet, the evolution of the dynamics and energy content of the jet can be described by the equations of conservation of momentum flux and energy flux. We assume that the jet velocity is non-relativistic, which is appropriate for the region of jet considered in this analysis. We consider a region of jet between distance  $l_1$  and  $l_2$  from the nucleus. The conservation of momentum flux,  $\Pi = \rho v^2 A$ , is described by:

$$\rho_2 v_2^2 A_2 = \rho_1 v_1^2 A_1 + \Pi_{buoy} \quad (15)$$

where  $\rho_{1,2}$ ,  $A_{1,2}$  and  $v_{1,2}$  are the gas density, cross-sectional area and velocity of the jet, respectively, and  $\Pi_{buoy}$  is the change in momentum flux due to the buoyancy force acting on the jet (see below).

The conservation of energy flux can be described by (cf. Bicknell 1994):

$$\left( \frac{1}{2} \rho_2 v_2^2 + U_2 + P_2 \right) v_2 A_2 = \left( \frac{1}{2} \rho_1 v_1^2 + U_1 + P_1 \right) v_1 A_1 \quad (16)$$

where  $P_{1,2}$  is the total internal pressure (assumed to match the external pressure at the given radius), and the internal energy terms,  $U_{1,2}$  are given by:

$$U_i = \frac{3}{2} P_i + U_e + U_B, \quad (17)$$

i.e. including terms for the internal energy carried by thermal particles, relativistic leptons and magnetic field, respectively.

With suitable initial conditions, the run of external pressure and of  $\kappa$  determined from the analysis in Section 3.2, Equations 15 and 16 can be solved for the unknowns  $\rho_2$  and  $v_2$  (where the mean particle mass  $\mu = 0.6$ , as appropriate for entrained ICM gas). The gas temperature of the thermal material is also determined via  $P_{therm,i} = (\rho_i/\mu m_H)kT_i$  where  $P_{thermal} = (2/3)U_{thermal} = (2\kappa_i/3)U_{E,i}$  is determined from the analysis in Section 3.2.

As discussed in Section 3.3 as initial conditions we assume  $v_{12kpc} = 6 \times 10^7 \text{ m s}^{-1}$ , and test a range of initial temperature values, which together with  $P_{12kpc}$  determine  $\rho_1$ . Equation 15 is rearranged for  $v_2$ , and then substituted into Equation 16. A standard root-finding algorithm can then be used to solve for  $\rho_2$ . The temperature of the thermal material in region 2 is then determined as explained above.

The buoyancy term  $\Pi_{buoy}$  in Equation 15 is determined as follows. The buoyant force acting on the jet material between  $l_1$  and  $l_2$  is given by:

$$F_{buoy} = -\Delta mg \quad (18)$$

where  $\Delta m$  is the mass of the surrounding material displaced by the chunk of jet material between  $l_1$  and  $l_2$ , i.e.  $\Delta m = \Delta m_{env} - \Delta m_{jet}$ , and  $g$  is the acceleration due to gravity:

$$g = \frac{Gm(l)}{l^2} \quad (19)$$

where  $m(l)$  is the enclosed gas mass within the galaxy cluster at radius  $l$ . In this case we can assume that  $\Delta m_{env} \gg \Delta m_{jet}$ , and so we take  $\Delta m = \Delta m_{env} = \rho_{env}(l)A(l)\delta l$ , where  $\rho_{env}(l)$  is the external gas density at distance  $l$ .

The change in momentum is given by:

$$\Delta p = F_{buoy}\Delta t \quad (20)$$

where  $\Delta t$  is the interval during which material travels from  $l_1$  to  $l_2$ . Hence  $\Delta l = v(l)\Delta t$ .

The change in momentum flux due to buoyancy is therefore:

$$\Pi_{buoy} = \Delta p v = \int_{l_1}^{l_2} F_{buoy} dl \quad (21)$$

Using the equation of hydrostatic equilibrium,  $F_{buoy}$  can be expressed in terms of the external pressure gradient:

$$F_{buoy} = -\frac{Gm(l)\rho_{env}(l)A(l)\Delta l}{l^2} = \frac{dP_{ext}}{dl}A(l)\Delta l \quad (22)$$

So

$$\Pi_{buoy} = \int_{l_1}^{l_2} \frac{dP_{ext}}{dl}A(l)dl \quad (23)$$

Hence the buoyancy term in Equation 15 can be evaluated using our measured external pressure gradient (e.g. Fig 1) and jet geometry.

Finally, the mass entrainment rate can be determined from conservation of mass flux as follows:

$$\rho_2 v_2 A_2 = \rho_1 A_1 v_1 + \Psi_2 \quad (24)$$

where  $\Psi_2$  is the mass entrained per unit time in the region between  $l_1$  and  $l_2$ .